Modeling of the Static Eccentricity Type of Fault in Squirrel Cage Induction Motor in COMSOL 6.0

Rakesh Deore[1], Gopinath Sengupta[2],Bipul Brahma[1], Shahrukh[1], Karuna Kalita[1]
1. Department of Mechanical Engineering, IIT Guwahati, Guwahati, Assam, India.
2. School of Energy Science and Technology, IIT Guwahati, Guwahati, Assam, India.

Abstract
Induction motors have wide applications in industries, so they are prone to faults, which later result in vibrations and hence noise. So it is important to analyze the faults in induction motors, their causes, and their effect on the system. Basically, there are so many faults in electrical machines due to mechanical as well as electrical means. Specifically, mechanical faults like bent rotor and stator, assembly misalignment, bearing faults, etc., result in an uneven air gap between the rotor and stator, called the eccentricity type of fault. These eccentricities are categorized as static eccentricity, dynamic eccentricity, and mixed eccentricity. In this paper, a 2D model of 60 slots, 48 rotor bars, and a 4-pole induction motor is modeled in the COMSOL 6.0 software. The concentric configurations are modeled and compared with different types of static eccentricities in the airgap. The unbalanced forces, airgap flux density, torque, and stator coil flux due to the different static eccentricities for the same configurations are analyzed and compared in the time domain as well as in the frequency domain.

Keywords: Electromagnetics, AC/DC Module, Induction Motor, Eccentricity, UMP.

Introduction
The rotating electrical devices possess the capability to transform mechanical energy into electrical energy, or conversely, convert electrical energy into mechanical energy. Specifically, a machine designed to convert electrical energy into mechanical energy through the generation process is referred to as a generator. Conversely, motors can transform mechanical energy into electrical energy through the motoring operation. Induction motors are the most commonly used electrical machines due to their robustness and reliability. Fig. 1 illustrates a typical cross-section of an induction motor.

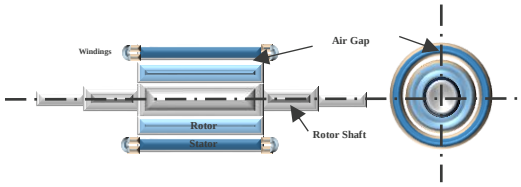

Figure 1: Cross Section of an Electric Machine with a Uniform Air-gap.

In flawless operation, the radial air gap between the rotor and the stator would ideally be uniform. However, due to various mechanical and electrical factors, the radial air gap becomes non-uniform [1]. Consequently, there is an eccentricity between the assembly of the rotor and stator. Induction machines operate based on the principle of electromagnetic induction, leading to an uneven distribution of the air gap flux. This asymmetry is most pronounced in the direction of the eccentricity [2]. The non-uniform radial air gap results in a pulling force exerted on the rotor in the direction of the eccentricity, known as Unbalanced Magnetic Pull (UMP).

Eccentricity serves as the primary cause of Unbalanced Magnetic Pull (UMP). However, aside from mechanical factors such as distorted shapes of rotor or stator cores, rotor bending, and bearing failures, electrical factors, like crawling and unbalanced rotor and stator currents, also contribute to variations in the air gap flux [1]. Consequently, unbalanced electromagnetic forces act on both the rotor and stator, resulting from these electrical and mechanical parameters. These unbalanced forces, in turn, generate vibrations and noise within the system. Mechanical balancing of the rotor and the utilization of mechanical dampers can be effective in reducing UMP. Additionally, employing electrical damper windings has proven to be a viable strategy. Research indicates that the use of a parallel winding type, rather than the series windings, is particularly effective in minimizing UMP in the induction motors [3]. Understanding the nature of the developed UMP concerning varying parameters is crucial for mitigating its effects. It is noteworthy that most electrical machine failures stem from mechanical faults, with eccentricity-related faults playing a significant role [1]. The statistics of motor faults, as depicted in Fig. 2, underscore the prevalence of eccentricity-related issues.

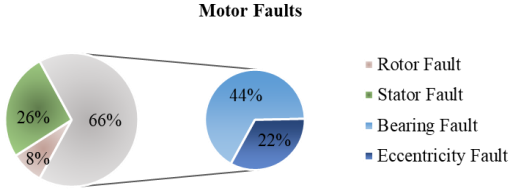

Figure 2: The Statistic of the Motor Faults.

The eccentricity faults are cyclic in nature, hence comprehending the development of UMP in relation to eccentricities becomes imperative for effectively addressing and reducing the associated impacts.

If the geometrical center-line of the rotor does not coincide with the geometrical center-line of the stator, a motor performs eccentric motion. There are three types of air gap faults diagnosed in electrical machines due to the three different eccentricities which are listed in the Fig. 3.

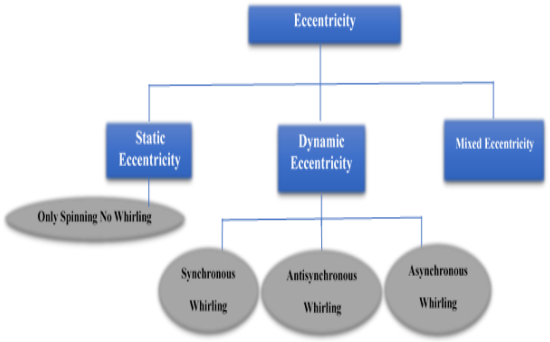

Figure 3: Types of eccentricities in an Electric Machine.

When the rotor rotates around its own geometric center, but there is a parallel offset between the geometric centers of the rotor and stator, it is referred to as static eccentricity. In this scenario, the rotor has only a spinning frequency. Conversely, in the case of dynamic eccentricity, the rotor axis is shifted parallel to the stator axis and also revolves around the stator's geometric center. In dynamic eccentricity, the rotor exhibits both a spinning frequency along its own center and a whirling frequency around the stator's geometric axis. If the rotor whirls with the same frequency of spinning then it is referred as synchronous whirling. If the rotor is whirling with a whirling frequency other than spinning frequency, it is known as the asynchronous whirling. Mixed eccentricity is a combination of both static and dynamic eccentricity. In this situation, the rotor axis is shifted parallel to the stator axis, but instead of revolving around the stator's geometric axis, the rotor whirls around a point other than it. In mixed eccentricity, a rotor can also have synchronous, asynchronous, or anti-synchronous whirling. To have proper insight into the eccentricity type of faults and its mitigation, it is necessary to understand this phenomenon.

In this paper, a 2D FEM model with defined constant out-of-plane thickness of the rotor and stator of the 60 slot and 48 bars, 4 pole, three phase double cage induction motor (shown in Fig. 4) is Modeled in COMSOL 6.0. The concentric as well as static eccentric models with different eccentricities are modeled for constant current coil excitation. For the same simulation parameters, the results for the different affecting parameters like stator coil concentrated flux, airgap flux w.r.t circumference of the airgap, UMP, and the point flux are compared for the concentric and the eccentric models.

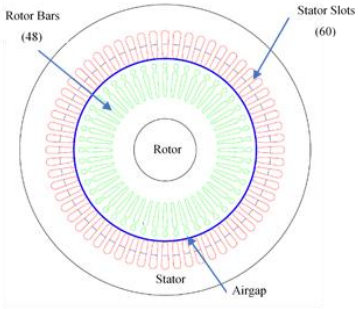

Figure 4: Rotor stator assembly

Modeling of the Induction Motor

Methodology for FEM

Maxwell's equations, Eq. (1-5), The electric fields density ($\vec{D}$) is not conserved and it is given by Gauss's law (Eq.1). The time derivative of the magnetic flux density ($\vec{B}$) can generate an electric field (Faraday's law, Eq.2). The Magnetic field can be split into conduction current and time derivative of electrical flux density, and given by Ampere's law (Eq.3). The magnetic field density is conserved and given by Eq.4. The Ohm's law at a point is given by Eq.5. These equations are combined in FEM software tools to find approximate solutions to the discretized finite elements.

$$\nabla \cdot \vec{D} = \rho \tag{1}$$

$$\nabla \times \vec{E} = -\frac{\partial \vec{B}}{\partial t} \tag{2}$$

$$\nabla \times \vec{H} = \vec{J} + \frac{\partial \vec{D}}{\partial t} \tag{3}$$

$$\nabla \cdot B = 0 \tag{4}$$

$$\vec{J} = \sigma \vec{E} \tag{5}$$

Where ρ is electric charge density, $\vec{E}$ is electrical field intensity, $\vec{H}$ is magnetic field intensity, $\vec{J}$ is the current density, and σ is electric conductivity.

For the electromagnetic problem, all the equations are combined and form the diffusion equation for moving conductors in their own frame of reference to calculate the spatial magnetic vector potential as

$$\sigma \frac{\partial \vec{A}}{\partial t} + (\nabla \times \vec{H}) = \frac{\sigma \Delta V}{d} + J^e \tag{6}$$

Where, $\vec{B} = \nabla \times \vec{A} = \mu \vec{H}$, ΔV is the potential difference, d is conductor length. μ is the magnetic permeability of the material.

The induction motor is an assembly of the rotor and stator where the airgap is present between them, as shown in Fig.4. For the FEM formulation the machine, the machine domain is divided into two sub-domains, stator includes the stator core, stator conductors, and some part of the airgap, whereas rotor has the combination of the rotor core, rotor bars and remaining part of the airgap. The eddy current effect of the stator conductors is neglected. In this modeling, though the rotor bars and winding are defined, but the rotor-stator circuit connecting to the windings is not inserted. The behavior of the machine cross-section is analyzed w.r.t the sinusoidal current input to the stator field i.e. to the winding arrangement coils. So the relevant equation is modified to, Eq. 7.

$$\nabla \times (\frac{1}{\mu_0 \mu_r} \nabla \times A) = J^e \quad (7)$$

The equation is solved for the out-of-the-plane magnetic vector component only which implies that the in-plane currents and out-of-the-plane magnetic fields are neglected. This is just the assumption for the 2D problem which greatly simplifies and stabilizes the problem.

Topology of the Geometry

The schematic in Figure 4 illustrates the cross-section of a squirrel cage induction motor. For modeling purposes, the induction motor assembly can be categorized into three integral parts: the stator, which serves as the primary body housing slots designed for accommodating winding coils known as stator windings; the rotor, comprising rotor bars and a shaft; and the air gap, denoting the open space situated between the rotor and the stator.

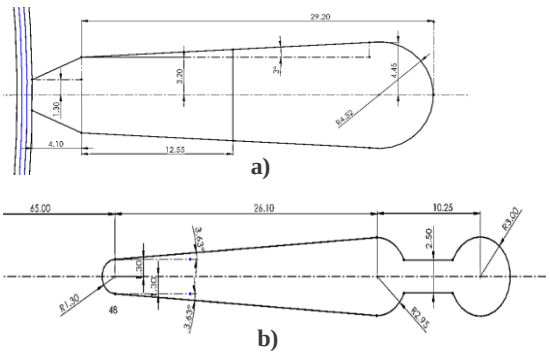

Figure 5: Dimensions of a) Stator Slot b) Rotor Bar.

Stator: The stator comprises two primary components: the stator core, constructed by stacking thin laminations of soft iron materials, and the winding arrangements inserted into the stator slots. In this configuration, the winding arrangement follows a parallel type, prompting the division of the stator slot into two segments to accommodate the parallel winding. The dimensions of the stator slots are detailed in Fig.5(a), while the specific dimensions of the actual machine can be found in Table 1 [5].

Rotor: The rotor assembly consists of the rotor core, rotor bars, and shaft. Similar to the stator core, the rotor core is constructed by stacking laminates of soft iron to mitigate eddy current losses. The rotor core features a closed single cage with 48 rotor slots, housing aluminum rotor bars in a designed arrangement and an aperture for fitting the stainless steel shaft. The dimensions of the rotor bars can be referenced in Fig.5(b)

Table 1: Dimensions of Machine [5].

Sr. No	Parameters	Values
1	No of Slots	60
2	No. of Bars	48
3	No of Poles	4
4	Supply Frequency (Hz)	50
5	No of Turns	33
6	Stator Outer Diameter (m)	0.354
7	Stator Inner Diameter (m)	0.223
8	Rotor Outer Diameter (m)	0.221
9	Length of Stator Core (m)	0.214
8	Coil Wire Diameter (mm)	1.22

Airgap: The radial airgap, with a width of 1 mm, is strategically modeled in three layers for the accurate assessment of flux distribution and the Unified Magnetic Potential (UMP) within the airgap. This modeling approach is crucial, considering that the airgap is divided into three equal parts (1:1:1) to optimize its representation.Each part of the airgap is assigned specific interactions: one part is modeled in conjunction with the stator to limit maximum eccentricity, ensuring that there is no interference between the stator and rotor. This approach guarantees an accurate depiction of the air gap. Simultaneously, another part is modeled with the rotor, acknowledging its rotational nature, thus ensuring the seamless integration of the main airgap with the stationary side. In the event of rotor eccentricity, the assembly, including the rotor and the portion of the airgap modeled with the rotor, will shift only within the allowable eccentricity region, aligning with the section of the airgap modeled with the stator. This meticulous modeling of the airgap, as illustrated in Fig.6, is imperative for addressing eccentricity concerns and maintaining the integrity of the overall motor assembly.

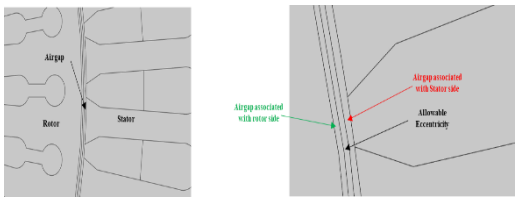

Figure 6: Modelling of Airgap.

Winding Arrangement

The winding arrangement is specifically designed for a balanced three-phase supply induction motor, as depicted in Fig.7. These windings are organized into four coil groups for each phase, resulting in a total of 12 coil groups for a parallel winding configuration. In the context of a 60-slot stator, the winding for each phase is further divided into two parallel paths to suit the characteristics of a 4-pole induction motor. This configuration employs a double-layered winding scheme distributed across the 60 slots, incorporating 120 conductors and forming 60 coils. The pole pitch extends over 15 slots, representing a span of 12 electrical degrees. Consequently, 5 slots per pole per phase. To ensure proper phasing, one phase spans over 10 slots and is positioned at a spacing of 120 degrees from the other phases. For instance, if the first coil of phase A is located in slot number 1, the B-phase coil would commence from slot number 11. Notably, the coil groups for each phase are positioned exactly opposite to each other, as illustrated in Fig.7.

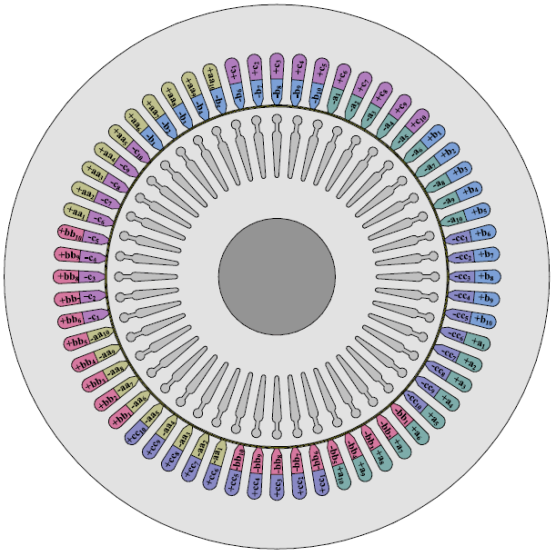

Figure 7: Schematic representation of Winding Scheme.

Each phase's coil groups are further subdivided into two parallel paths, with each path containing two coil groups. The coil groups placed opposite to each other are connected in opposite parallel. To complete the circuit, one end of all three phases of the winding is interconnected to form a star point, while the other three ends are linked to a balanced three-phase supply.

Steps in COMSOL Modeling

To conduct a comprehensive electromagnetic analysis of the machine, a dedicated AC/DC physics module and an electric circuit have been integrated into the COMSOL Multiphysics model. The Rotating Machinery, Magnetics (rmm) module within COMSOL Multiphysics allows for both time-dependent and stationary studies. The Finite Element Method (FEM) approach is employed to derive a solution for the given problem. The model is constructed using 2D geometry tools in COMSOL Multiphysics. The stator and rotor components are defined with appropriate materials, as outlined in Table 2. The assembly is created using an identity pair. The rotor part introduces rotational motion, and a moving mesh with a constant rotating frequency is assigned to the rotor. Continuity is established for the identity pair.

Table 2: Material Assigned to Different Parts.

Sr. No	Parts	Material Assigned
1	Stator Core	Soft Iron
2	Rotor Core	Soft Iron
3	Air Gap	Air
4	Coils	Copper
5	Rotor bars	Aluminium
6	Shaft	SS303

A proper definition of boundary conditions is crucial. Magnetic insulation is applied at the external boundary of the domain, corresponding to the outer boundary of the stator core. Initial values for the magnetic vector potential are set in accordance with the specific electric machine under simulation. In the case of an induction machine, all initial values for magnetic vector potentials are set to zero. Coils are configured based on the winding arrangement, as depicted in Fig. 7. In this study, the machine is modeled with a sinusoidal current input of 5A to each phase, with a phase difference of 120 degrees applied to the coils. The time-dependent study is executed for a duration of 0.1 seconds. The relative permeability of the soft iron is specified as 1000.

To incorporate static eccentricity, it is imperative to establish a user-defined cylindrical coordinate system. Furthermore, for effective post-processing, defining domain integration becomes crucial. In examining the electromagnetic force and torque resulting from static eccentricity, the rotor domain is specifically chosen for force computation, while the torque calculation focuses on the appropriate air gap. To address these considerations, a physics-controlled mesh is generated for the system, utilizing triangular quadratic elements, as illustrated in Fig. 8. The mesh details, encompassing the number of elements per part and mesh quality, are meticulously outlined in Table 3.

This approach ensures a targeted and accurate analysis of the developed electromagnetic force and torque arising from static eccentricity. The use of a physics-controlled mesh with triangular quadratic elements enhances the precision of the simulation, aligning with the specific requirements of the study. By implementing these specifications and utilizing the FEM approach, this simulation aims to provide a

comprehensive analysis of the electromagnetic behavior of the machine under the defined operating conditions.

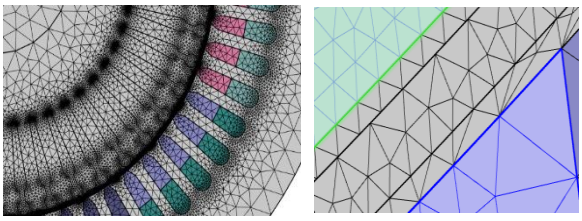

Figure 8: Mesh Used in Simulation.

Table 3: The Mesh Quality and No of Elements per Part.

Parts	No of Elements	Min. Mesh Quality	Avg. Mesh Quality
Stator Core	18846	0.4944	0.789
Rotor Core	45506	0.4154	0.799
Air Gap	16238	0.1107	0.7032
Stator slots	133	0.648	0.8284
Rotor bars	334	0.6408	0.8399
Shaft	124	0.7307	0.8501

Result and Discussion

The 2D electromagnetic behavior of the induction motor was modeled by following the outlined steps. A sinusoidal current input of 5A was applied to each phase with a phase difference of 120 degrees, and the circuit equation bridge-off condition was excluded. Initially, the simulation focused on the concentric rotor-stator assembly. Subsequently, the model incorporated the effect of eccentricity between the rotor and stator, specifically for the static eccentricity case, considering varying eccentricities.

Two scenarios were simulated: one with a concentric rotor and the other with the rotor operating under static eccentricity conditions. A comparison of the results aimed to elucidate the impact of static eccentricity on various parameters, such as currents and voltages in the stator coils, flux density through the air gap, and the magnitude of unbalanced magnetic pull (UMP) acting on the rotor. The analysis spanned different levels of static eccentricity, ranging from 5% to 99.5% at intervals of 5%. The objective was to discern the influence of static eccentricity on the aforementioned parameters. The findings shed light on how the motor's performance varied under different static eccentricity conditions.

Magnetic Flux Density

Fig.9 and Fig.10 illustrate the distribution of magnetic flux density at a specific time instant (t=0.1 sec) on the surfaces of the concentric rotor and the rotor with 10% static eccentricity, respectively. The total air-gap width is 1 mm, and a static eccentricity of 10% of the total air-gap, equivalent to 0.1 mm, is applied in the X direction. The flux density across the surface reveals the formation of two pole pairs. The rotor rotates at a nominal speed of 1425 rpm. A sinusoidal current of 5A is supplied with a phase difference of 120 degrees to each phase at a supply frequency of 50 Hz.

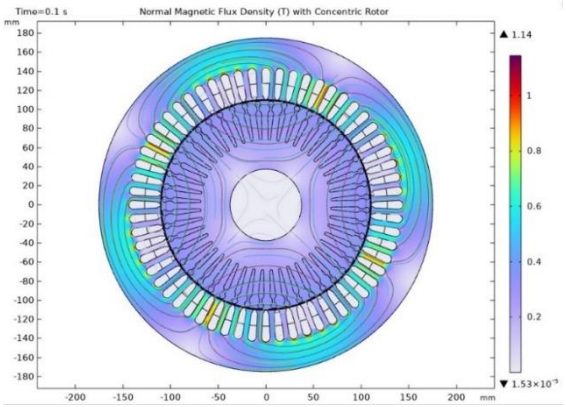

Figure 9: Magnetic Flux Density with Concentric Rotor.

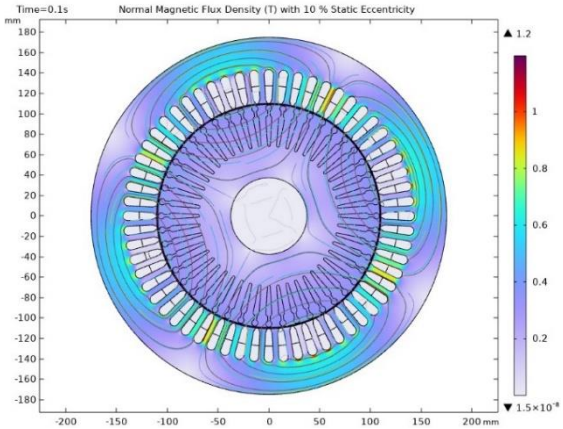

Figure 10: Magnetic Flux Density with 10 % Static Eccentric Rotor.

In Fig.11 the current profiles for each phase are depicted. These profiles are based on the 5A sinusoidal current input at a phase difference of 120 degrees, corresponding to a supply frequency of 50 Hz. The rotor's rotational motion at 1425 rpm is considered in these simulations.

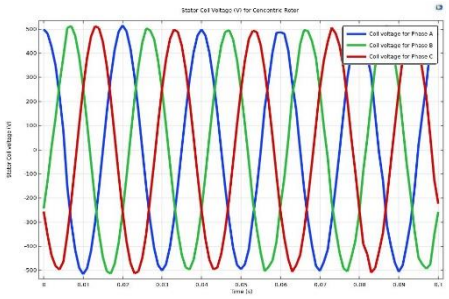

Figure 11: Current Profile in Coils with Concentric Rotor and 10 % Static Eccentric Rotor.

Voltage Profile

Upon supplying a sinusoidal current of 5A with a phase difference of 120 degrees to each phase, the stator coil voltage profiles are depicted in Fig.12 (a) and Fig.12 (b) for each phase, considering a supply frequency of 50 Hz. It is observed that the stator coil voltage for the concentric rotor is approximately 515V. Maintaining all other computational parameters constant, except for eccentricity, the stator coil voltage for the rotor with 10% eccentricity, resulting from the 5A current supply to the star-connected BCW induction motor, is approximately 463V. This distinction is evident in Fig.13 which provides a comparative analysis of the voltage produced in the stator coil for both the concentric and 10% eccentric rotor configurations, specifically focusing on phase A.

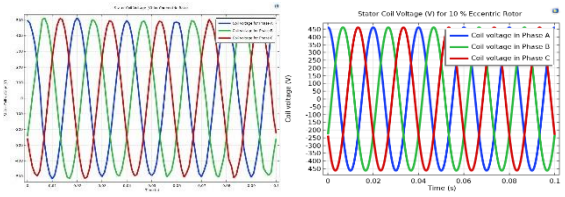

a) **b)**

Figure 12: a) Voltage Profile in Coils with Concentric Rotor b) Voltage Profile in Coils with 10% Static Eccentric Rotor.

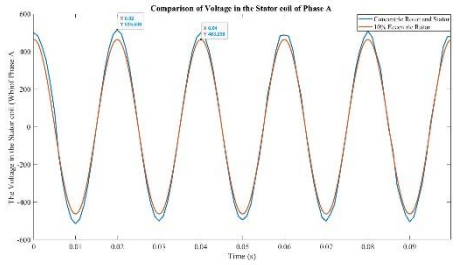

Figure 13: Comparison of the Stator Coils Voltage in Concentric Rotor & 10% Static Eccentric Rotor for Single Phase A.

Stator Coil Flux

In the same configuration, the flux generated in each phase of the coil for both the concentric and 10% static eccentricity cases is illustrated in Fig.14.(a) and Fig.14.(b) respectively. Specifically, the stator coil flux produced in Phase A, Phase B, and Phase C is presented in these figures. Notably, there is a reduction in the flux produced in each stator coil per phase, decreasing from 1.5901Wb to 1.47517Wb. The comparative analysis of this stator coil flux is depicted in Fig.15 considering a current supply of 5A at a frequency of 50 Hz. This figure provides a visual representation of the contrast in stator coil flux between the concentric and 10% eccentric rotor configurations.

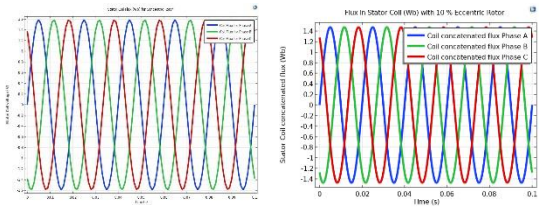

a) **b)**

Figure 14: a) Flux Profile in Coils with Concentric Rotor b) Flux Profile in Coils with 10% Static Eccentric Rotor.

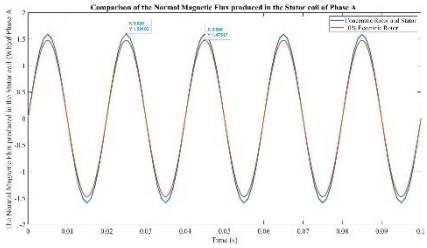

Figure 15: Comparison of the Stator Coils Voltage in Concentric Rotor & 10% Static Eccentric Rotor for Single Phase A.

Air gap Flux Density

Among all the aforementioned results, our primary focus lies in the variation of airgap flux density. Given the presence of eccentricity in the rotor-stator assembly, it is crucial to compare the variation in airgap parameters with the concentric configuration. The impact of eccentricity on the rotor-stator assembly is ultimately reflected in the airgap, and the airgap flux serves as an indicator of pole formation in the machine. A stationary study was conducted to plot the variation of airgap flux concerning arc length and angular position. Fig.16 and Fig.17 provide a comparison of airgap flux variation in the concentric rotor and eccentric rotor concerning arc length and angular position, respectively. The airgap flux is measured on the inner boundary of airgap layer 2, which comprises four arcs to form a circle with a radius of 109.5 mm. Each arc corresponds to 90 mechanical degrees.

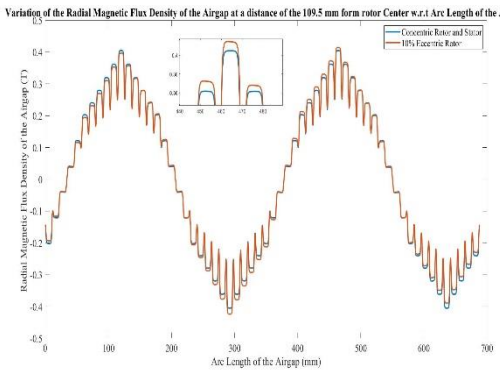

Figure 16: Comparison of Airgap flux density in Concentric Rotor & 10% Static Eccentric Rotor w.r.t Arc Length of the Airgap Layer 2.

Referring to Fig.16, as static eccentricity is applied along the X-axis (in the 1st quadrant, positive X-axis), and the machine rotates counterclockwise, it is observed that in the first positive half cycle of the air-gap flux density, where the air-gap is minimum due to eccentricity, the flux density with an eccentric rotor has a higher peak value than the concentric one. Conversely, for the second half cycle, the peak value for the eccentric rotor is lower than that for the concentric one. The distortion in the flux density waveform is attributed to slot harmonics, as verified by Fig.17. Here, it can be seen that the width of one peak is equal to 60, which corresponds to the angle covered by the area of one stator slot, considering the presence of 60 stator slots.

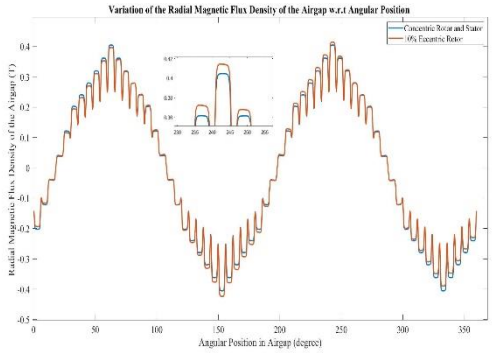

Figure 16: Comparison of Airgap flux density in Concentric Rotor & 10% Static Eccentric Rotor w.r.t Angular Position.

In Fig.17 (a) and Fig.17 (b), on the same layer 2, the point-normal airgap flux density (T) is plotted at points on the side of the maximum airgap and the minimum airgap for the concentric rotor and 10% eccentric rotor, respectively. It is evident that in the case of the concentric rotor, the airgap flux density at these points and locations is uniform, reflecting no airgap distortion.

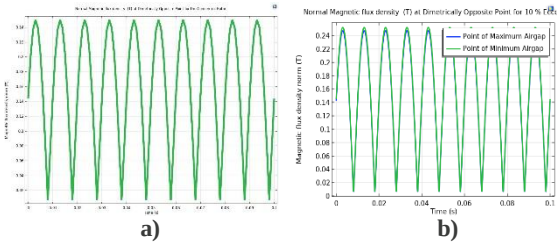

a) **b)**

Figure 17: Comparison of Airgap flux density in Concentric Rotor & 10% Static Eccentric Rotor w.r.t Angular Position.

However, for the 10% eccentric rotor at the same points, the flux density is maximal in the direction of the minimum airgap and minimal in the direction of the maximum airgap. The magnitude of the airgap flux density at these points in the concentric rotor is 0.4T, while for the 10% eccentric rotor, the magnitude at a point in the direction of the minimum airgap is 0.423T, and in the direction of the maximum airgap, it is 0.389T.

This non-uniformity in the airgap flux density in the concentric rotor due to eccentricity leads to the development of additional forces on the rotor, resulting in an unbalanced and unstable system. This additional unbalanced force is referred to as the Unbalanced Magnetic Pull (UMP).

Unbalanced Magnetic Pull (UMP)

As discussed in earlier sections, Unbalanced Magnetic Pull (UMP) arises from the uneven distribution of flux in the airgap. Due to eccentricity, the flux distribution becomes non-uniform, leading to the development of additional pulling forces in the system. Fig.18 (a) and Fig.18 (b), compare the unbalance force on the rotor for the concentric rotor and the 10% eccentric rotor, respectively.

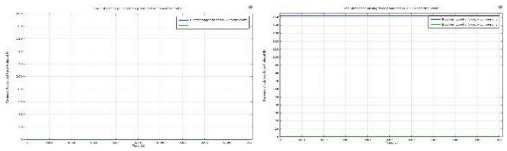

a) **b)**

Figure 18: Comparison of UMP in a) Concentric Rotor b) 10% Static Eccentric Rotor.

In the case of a perfectly aligned configuration, this force is negligible or effectively 0 N. However, for the eccentric rotor, in the direction of eccentricity (in our case, only in the +ve X direction), the maximum magnitude of the unbalanced force is 152.0 N, while in the Y direction, it is 0 N, as no eccentricity is applied in that direction. Figures 3.18a and 3.18b depict the Fast Fourier Transform (FFT) analysis of the UMP in the concentric rotor and the 10% eccentric rotor, respectively. Inherent to parallel winding, there is a force component at 2fs (here 100 Hz). Due to static eccentricity, two force components emerge at 0 Hz and 2fs (here 100 Hz), as clearly illustrated in Fig.19 (a) and Fig.19 (b).

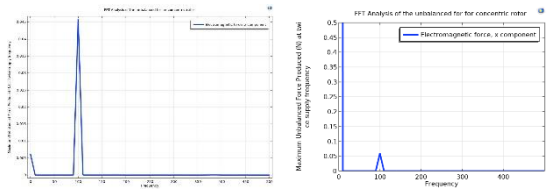

a) **b)**

Figure 19: Comparison of FFT of UMP in a) Concentric Rotor b) 10% Static Eccentric Rotor.

Subsequent simulations were conducted for a range of eccentricity percentages, spanning from 5% up to 99.5%, with increments of 5%. The impact of these varying degrees of eccentricity on several parameters was analyzed. The assessment included the examination of different eccentricities concerning stator coil flux, airgap flux density at a specific point on layer 2 in the directions of minimum and maximum airgap, and the Unbalanced

Magnetic Pull (UMP) in the system attributed to static eccentricity at frequencies of 0 Hz and $2f_s$ (twice the supply frequency).

Variation of the Stator Coil Flux w.r.t % of Static Eccentricty: The presented Fig.20 illustrates the change in stator coil flux concerning the percentage of eccentricity, ranging from 5% to 99.5% in the air gap. The current supply is maintained at 5A with a frequency of 50 Hz. Observations indicate a notable increase in stator coil flux, progressing from 1.474 Wb at 5% eccentricity to 1.83 Wb at 99.5% eccentricity.

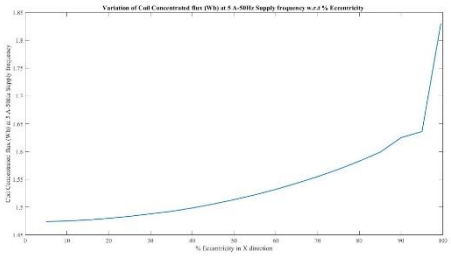

Figure 20: Variation of Stator Coil Flux w.r.t % Eccentricity

Variation of Airgap Flux Density w.r.t % of Static Eccentricty: Fig.21 and Fig.22 depict the variation in airgap flux density concerning the percentage of eccentricity, ranging from 5% to 99.5% in the airgap. The current supply is maintained at 5A with a frequency of 50 Hz, and the analysis is conducted in the directions of both the minimum and maximum air gaps resulting from the eccentricity.

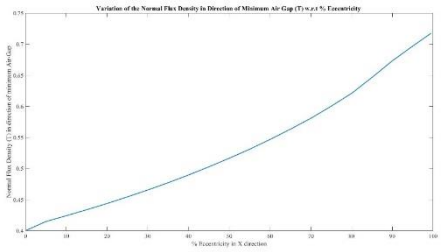

Figure 21: Variation of Airgap Flux Density w.r.t % Eccentricity in Direction of the Minimum airgap.

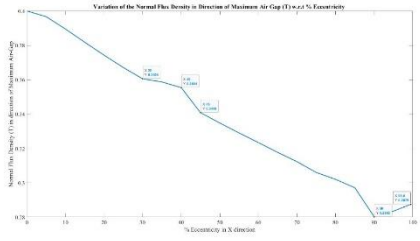

Figure 22: Variation of Airgap Flux Density w.r.t % Eccentricity in Direction of the Maximum Airgap.

As previously discussed, for a specific eccentricity, the airgap flux density is expected to be higher in the case of the minimum airgap and vice versa. In the direction of the minimum airgap, it is observed that as the eccentricity increases, the airgap flux density also increases. Specifically, it rises from 0.414 T at 5% eccentricity to 0.7173 T at 99.5% eccentricity. Conversely, in the direction of the maximum airgap, an increase in eccentricity leads to a decrease in airgap flux density. It decreases from 0.3967 T at 5% eccentricity to 0.2875 T at 99.5% eccentricity.

Variation of UMP w.r.t % of Static Eccentricty: As previously discussed, static eccentricity introduces a component of unbalanced force at two harmonics, one at 0 Hz and the other at $2f_s$ (in this case, 100 Hz). Fig.23 and Fig.24 illustrate the variation of Unbalanced Magnetic Pull (UMP) obtained from Fast Fourier Transform (FFT) concerning the percentage of eccentricity at 0 Hz frequency and at the $2f_s$ frequency (100 Hz), respectively.

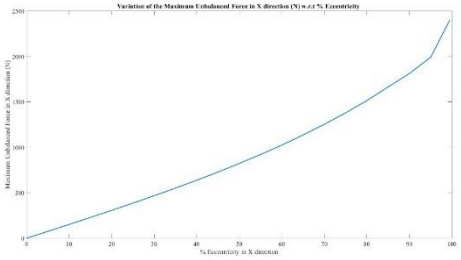

Figure 23: Variation of UMP w.r.t % Eccentricity at 0 Hz.

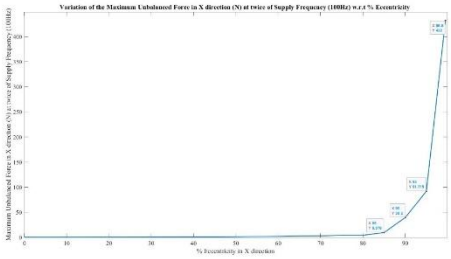

Figure 22: Variation of UMP w.r.t % Eccentricity at 100 Hz (twice the Supply Frequency f_s)

With an increase in static eccentricity, there is a corresponding increase in the unbalanced force at both harmonics. In the case of the concentric configuration, the unbalanced force was 0 N. However, as the eccentricity increases from 5% to 99.5%, the unbalanced force rises from 76 N to 2400 N at 0 Hz. Similarly, for the 100 Hz frequency, the unbalanced force increases from 0.048 N at 5% eccentricity to 432 N at 99.5% eccentricity.

In the simulation of the four-pole induction motor, it is observed that the maximum flux density in the eccentric rotor cross-section is 5.263% greater than that in the concentric cross-section for both the concentric rotor and the 10% eccentric rotor configurations. The voltage produced in the stator coil with a 10% eccentric rotor is found to be 10.1% lower than the voltage produced in the 0% eccentric rotor configuration. The normal flux in the stator coils of the concentric rotor is 7.24% greater than the

normal flux in the stator coils of the 10% eccentric rotor. The airgap flux density at the minimum airgap is 7.5% greater than that of the concentric rotor, while the airgap flux density at the maximum airgap is 5.25% lower than that of the concentric rotor. The airgap flux density in the direction of the minimum airgap is 8.74% higher than that in the direction of the maximum airgap.

Conclusion

A 2D model of a 60-slot, 48-rotor-bar, 4-pole induction motor has been simulated in COMSOL 6.0. A sinusoidal current with a magnitude of 5 A at a supply frequency of 50 Hz is applied as input, with a phase difference of 120 degrees per phase. The analysis explores the effects of eccentricity on various parameters such as stator coil voltage, stator coil flux, airgap flux, and Unbalanced Magnetic Pull (UMP). The following conclusions can be drawn from the study:

1. The airgap flux density in the airgap layer is uniform for the concentric rotor-stator assembly, but eccentricity introduces non-uniformity in the airgap flux density for the eccentric rotor.
2. No unbalance force is observed in the case of the concentric rotor and stator. However, static eccentricity introduces unbalanced forces at 0 Hz and 100 Hz frequencies. The constant component at 0 Hz frequency has a significant magnitude of 150 N in the case of the 10% eccentric rotor.
3. As rotor eccentricity increases, the formation of stator coil flux also increases.
4. With increasing eccentricity, the airgap flux in the direction of the minimum airgap increases, while in the direction of the maximum airgap, it decreases.
5. The constant component of UMP at 0 Hz and another component at twice the supply frequency both increase as eccentricity increases [6].

References

1. Salah, D. G. Dorrell, and Y. Guo, “A review of the monitoring and damping unbalanced magnetic pull in induction machines due to rotor eccentricity,” in *IEEE Transactions on Industry Applications*, May 2019, vol. 55, no. 3, pp. 2569–2580. doi: 10.1109/TIA.2019.2892359.
2. J. Faiz, B. M. Ebrahimi, and M. B. B. Sharifian, “Different faults and their diagnosis techniques in three-phase squirrel-cage induction motors-a review,” *Electromagnetics*, vol. 26, no. 7, pp. 543–569, Oct. 2006, doi: 10.1080/02726340600873003.
3. A. Burakov and A. Arkkio, “Comparison of the unbalanced magnetic pull mitigation by the parallel paths in the stator and rotor windings,” *IEEE Transactions on Magnetics*, vol. 43, no. 12, pp. 4083–4088, Dec. 2007, doi: 10.1109/TMAG.2007.906885
4. J. Martinez, A. Belahcen, and A. Arkkio, “A 2D FEM model for transient and fault analysis of induction machines,” in Przeglad Elektrotechniczny, 2012, pp. 157-160.
5. R. Deore, B. Brahma, Shahrukh, and K. Kalita, “The Passive Vibration Control in Bridge Configured Winding Cage Rotor Induction Motor: An Experimental Analysis”, International Conference on Rotordynamics, https://doi.org/10.1007/978-3-031-40455-9.
6. D. Guo, F. Chu, and D. Chen, “The unbalanced magnetic pull and its effects on vibration in a three-phase generator with eccentric rotor,” *Journal of Sound & Vibrations*, vol. 254, no. 2, pp. 297–312, Jul. 2003, doi: 10.1006/jsvi.2001.4088.

Acknowledgments

The authors gratefully acknowledge to Government of India for the availability of the COMSOL Multiphysics 6.0 software through the ISTEM India platform.